Improved Mean Field Estimates of GEMS AOD L3 Product: Using Spatio-temporal Variability

Sooyon Kim[1], Yeseul Cho[3], Hanjeong Ki[1], Seyoung Park[1], Dagun Oh[1], Seungjun Lee[1], Yeonghye Cho[1], Jhoon Kim[3], Wonjin Lee[4], Jaewoo Park[1,2], Ick Hoon Jin[1,2], and Sangwook Kang[1,2]

[1]Department of Statistics and Data Science, Yonsei University, Seoul, Republic of Korea
[2]Department of Applied Statistics, Yonsei University, Seoul, Republic of Korea
[3]Department of Atmospheric Sciences, Yonsei University, Seoul, Republic of Korea
[4]Environmental Satellite Center, National Institute of Environmental Research, Ministry of Environment

Correspondence: Jaewoo Park (jwpark88@yonsei.ac.kr), Ick Hoon Jin (ijin@yonsei.ac.kr), and Sangwook Kang (kanggi1@yonsei.ac.kr)

Abstract. This study presents advancements in the processing of satellite remote sensing data, focusing mainly on Aerosol Optical Depth (AOD) retrievals from the Geostationary Environment Monitoring Spectrometer (GEMS). The transformation of Level 2 (L2) data, which includes atmospheric state retrievals, into higher-quality Level 3 (L3) data is crucial in remote sensing. Our contributions lie in two novel improvements to the processing algorithm. First, we improve the inverse distance weighting algorithm by incorporating quality flag information into the weight calculation. By assigning weights inversely proportional to the number of unreliable grids, the method can provide more accurate L3 products. We validate this approach through simulation studies and apply it to GEMS AOD data across various regions and wavelengths. The use of the quality flags in the algorithm can provide a more accurate analysis in remote sensing. Second, we employ a spatio-temporal merging method to address both spatial and temporal variability in AOD data, a departure from previous approaches that solely focused on spatial variability. Our method considers temporal variations spanning previous time intervals. Furthermore, the computed mean fields show similar spatio-temporal patterns to the previous studies, confirming that they can capture real-world phenomena. Lastly, utilizing this procedure, we compute the mean field estimates for GEMS AOD data, which can provide a deeper understanding of the impact of aerosols on climate change and public health.

1 Introduction

In satellite remote sensing missions, observed data is processed at different levels. Using retrievals of the atmospheric state (Level 2; L2), L2 AOD products are regridded into Level 3 (L3) going through the process of filling gaps and filtering out noises (Cressie, 2018). We first introduce the theoretical background of the mean fields algorithm for generating L3 data application to aerosol optical depth (AOD) retrievals from the Geostationary Environment Monitoring Spectrometer (GEMS) ~~satellite~~instrument. We consider an oversampling method for generating L3 AOD data, inverse distance weighting (IDW), and a modified mean field algorithm with consideration to spatio-temporal variability of AOD data in the algorithm.

Aerosols play a critical role in radiative forcing, climate change, and air quality (Brauer et al., 2015; Charlson et al., 1992; Stocker, 2014; Kaufman et al., 2002). Directly, they change the planetary albedo by reflecting solar radiation and absorbing terrestrial radiation, affecting the radiation balance. Indirectly, as cloud condensation nuclei, aerosols modify cloud properties and increase cloud droplet concentration, impacting solar radiation and cloud albedo (Alexander et al., 2013). Aerosol affects human health and air quality, especially in the regions affected by long-range transport or the regions with heavy aerosol emissions due to rapid industrialization and high population density. Those are linked to cardiovascular, respiratory, and allergic diseases, and even increased mortality rates (Pöschl, 2006; Tager, 2013).

Additionally, high aerosol concentrations can severely reduce visibility, leading to hazardous weather conditions like haze, smog, and dust storms (Charlson, 1969; Chen and Tsai, 2001). Thus, understanding aerosols' multifaceted impacts is crucial for addressing climate change, public health, and environmental visibility issues. The distribution of aerosols is characterized by their complexity, leading to increased uncertainty in determining aerosol radiative forcing effects (Chen et al., 2022). Analyzing aerosol's spatio-temporal distribution remains crucial for developing air pollution control policies and understanding the climate impacts of aerosols. Although accurate Aerosol Optical Properties (AOPs) and their vertical profiles can be obtained from ground-based measurements at the high temporal resolution, their AOPs can represent local-scale variability of limited spatial coverage. Unlike ground-based instruments, the regional and global monitoring of AOPs has been conducted by using satellite measurements.

A previous study of Park et al. (2023) focused on AOD retrievals by considering spatial variability. Specifically, Park et al. (2023) used the IDW algorithm to regrid L2 products and estimated the mean field of L3 products by considering spatial variability. Compared to the previous work, we have the following contributions. First, we have integrated quality flag information in the IDW algorithm so that we can rule out unreliable grid points. In this study, we employ the IDW algorithm to compute mean field estimates for AOD data. The IDW method is a widely used gap-filling algorithms that imputes missing observations through a linear combination of neighboring observations. Integrating quality flags (QF) as weights on IDW algorithm allows quantitative assessment of the influence of data itself from various quality levels on the final product. It can mitigate the impact of low-quality data and lead to lower MSE when implementing the IDW algorithm, as proven in Section 4. By considering variability in L2 AOD products, we can obtain more reliable L3 AOD products in this step. Second, we use the spatio-temporal merging method (Kikuchi et al., 2018) to obtain L3 AOD mean field estimates. We first compute Numerous studies have demonstrated that aerosol optical depth (AOD) exhibits significant spatio-temporal variabilities and use them to filter out uncertain values variability due to natural and anthropogenic factors. This is particularly evident in regions like northwestern China, where understanding the spatio-temporal dynamics is essential for effective atmospheric pollution management and control, as aerosol concentrations are heavily influenced by seasonal and graphical variations (Zhang, 2023). Moreover, the characteristics of the data collection device, the satellite, play a crucial role. The AOD data analyzed in this study is obtained from the Geostationary Environment Monitoring Spectrometer (GEMS). When collecting data using such devices, it is imperative to consider spatio-temporal variability to ensure the high-quality of aerosol data. For instance, a study conducted in East Asia optimized the spatio-temporal ranges used for validating satellite products, such as total ozone and NO2, by leveraging long-term data from both ground-based and satellite observations (Park et al., 2020). Incorporating

quality flag information can reduce the influence of low-quality data on the IDW algorithm, resulting in lower MSE, as we demonstrated in our simulation study. Nevertheless, it remains crucial to identify and exclude pixels with unreliable AOD values, as they can introduce substantial uncertainties in mean field estimates. In our analysis, we apply a filter to remove pixels with a cloud radiance fraction (CRF) exceeding 0.4, ensuring that the included AOD values are not significantly impacted by cloud contamination. We observe that our method can provide more ~~realistic mean field estimates compared to the work Park et al. (2023) only considering spatial~~ smoother AOD surfaces than the simple averaging method without considering spatio-temporal variability.

The outline of the remainder of this manuscript is as follows. In Section 2, we describe the GEMS data used in our analysis. In Section 3, we describe our method to compute the mean field of L3 AOD products. In Section 4, we conduct simulation studies to validate our method. We apply the proposed method to GEMS data in Section 5. We conclude with a discussion in Section 6.

2 GEMS Data

GEMS is the first UV-Vis hyperspectral satellite instrument onboard the Geostationary Korea Multi-Purpose Satellite-2B (GK-2B), launched on February 19, 2020. Its mission is to monitor air quality across Asia (5°S–45°N, 75–145°E) with high temporal (1-hour) and spatial resolution (3.5×7.7 km^2 at Seoul, South Korea), using hyperspectral measurements in the 300–500 nm range.

The GEMS aerosol retrieval (AERAOD) algorithm retrieves AOD, single scattering albedo (SSA), and aerosol layer height (ALH) using GEMS L1 data from six wavelengths (354, 388, 412, 443, 477, and 490 nm). This algorithm solves the limited degree of freedom for signal problems in the GEMS wavelength range by using two-channel inversion to retrieve the initial guesses of AOD and SSA and then inputting them into the optimal estimation method. This retrieval method was tested with sensitivity in the UV-Vis region to aerosol absorption and with Ozone Monitoring Instrument (OMI) Level 1 data (Kim et al., 2018; Go et al., 2020a, b). Initially developed from synthetic OMI data by Kim et al. (2018) and Go et al. (2020b), the operational version was later improved by Cho et al. (2023) based on real GEMS Level 1 data. An update to the aerosol algorithm, Version 2.0, was released in November 2022, which included reprocessing earlier data.

In this study, the following variables are used for calculating L3 AOD mean fields (Table 1).

Additional to Solar Zenith Angle (SZA) and Viewing Zenith Angle (VZA), due to the unavailability of cloud fraction in the GEMS AOD product, we utilize the GEMS L2 cloud product as masking criteria. The GEMS L2 cloud product is obtained from the GEMS cloud retrieval algorithm (Kim et al., 2024). With the same hyperspectral measurement range, temporal and spatial resolution as the AERAOD algorithm, the GEMS cloud retrieval algorithm retrieves the effective cloud fraction (ECF) and provides the cloud ~~radiation~~ radiance fraction (CRF) via the CRF conversion process (Choi et al., 2020).

To filter out pixels biased with high cloud fraction, we leverage CRF with wavelength corresponding to AOD product.

Table 1. Description of the variables for GEMS L2 AERAOD data.

Group	Variable
Data Fields	AOD at wavelength of ~~354nm, 443nm, 550nm~~ 354 nm, 443 nm, 550 nm
	16-bit Quality Flag
Geolocation Fields	Longitude
	Latitude
	Solar Zenith Angle
	Viewing Zenith Angle

3 Methodology

We apply a three-stage procedure to calculate the mean field of the L3 AOD products. First, we regrid L2 AOD products using the IDW method with neighboring spatial information to obtain the L3 AOD products. Then merge the L3 AOD products by considering spatio-temporal variability in the products according to Kikuchi et al. (2018). Specifically, we merge the L3 AOD products using the previous T time products from the target products of interest. Lastly, we produce the mean field of the L3 AOD products by taking a simple mean of the spatio-temporally merged L3 data. The outline of the method is illustrated in Figure 1.
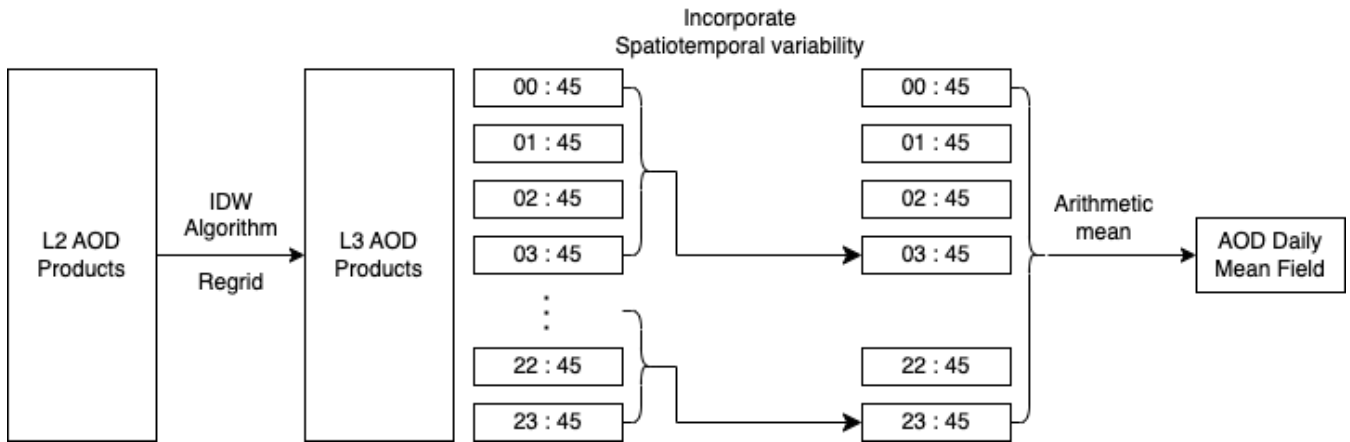
Figure 1. Illustration of the proposed estimation of the mean field methods under the window size of $T = 3$.

3.1 Inverse Distance Weighting

In this section, we describe the inverse distance weighting (IDW) algorithm that can obtain L3 AOD products. Several methods, including the nearest neighbor method (Lotrecchiano et al., 2021), the linear interpolation method (Abdullah et al., 2019; Shepard, 1968) and the spline interpolation method (Kuhlmann et al., 2013), have been proposed to interpolate the air quality

mass. The IDW algorithm (Zimmerman et al., 1999) is one of the most popular methods among the linear interpolation methods due to its computational simplicity. Our goal is to obtain the L3 AOD products for each longitude-latitude location.

Let (x_0, y_0) be the target longitude-latitude location for calculating the L3 AOD product. Suppose $(x_1, y_1), \cdots, (x_n, y_n)$ represent the neighboring longitude-latitude locations to (x_0, y_0), each paired with its respective L2 AOD product denoted by $\text{AOD}(x_1, y_1), \cdots, \text{AOD}(x_n, y_n)$. To calculate the L3 AOD product in our application, we use grid points within the ~~r-radius~~ fourth-order neighbor of (x_0, y_0). This means that, for the given (x_0, y_0), we use the locations that satisfy $x_i \in (x_0 - r, x_0 + r)$ and $y_i \in (y_0 - r, y_0 + r)$. Specifically, we set the ~~radius r~~ resolution at 0.1 ° for the East Asia region and 0.05° for the Korean Peninsula region. Then, for the fixed observed time point t_0, the IDW estimate is

$$\text{AOD}_{IDW}(x_0, y_0, t_0) = \sum_{i}^{n} \lambda_i \text{AOD}(x_i, y_i, t_0), \tag{1}$$

where the weight of each location is defined as

$$\lambda_i = \frac{1/d_i^p}{\sum_{i}^{n} 1/d_i^p}. \tag{2}$$

In ~~Equation~~ Eq. (2), d_i is the Euclidean distance from (x_0, y_0) to (x_i, y_i) and p is the power parameter. Therefore, ~~Equation~~ Eq. (1) is based on the weighted average of the L2 AOD values from neighboring locations; the larger weight is assigned to grid points close to the location of interest x_0.

Depending on the choice of p, the IDW estimates ~~yields~~ yield different outcomes. As p goes to 0, ~~Equation~~ Eq. (2) becomes equal weight and the IDW estimate gets close to a simple average from neighboring locations. On the other hand, as p goes to ∞, the larger weight is concentrated on the locations near x_0 and the IDW estimate converged to the estimate obtained through the nearest neighbor. Although the optimal choice of p can be different depending on the study (Liu et al., 2006), $p = 2$ is the most commonly used value since when $p = 2$, the weight for distance between grid points decays relatively faster to avoid the discontinuity (Webster and Oliver, 2007). Following this convention (Isaaks and Srivastava, 1989), we also use $p = 2$ in our analysis.

3.1.1 An Enhanced Inverse Distance Weighting with Quality Flag Information

A quality flag is an indicator that contains data quality information for each grid points. Such an indicator is widely used for data cleaning and selection. In our study, we have quality flag information in the L2 AOD products (coded as a 16-bit unsigned integer value). The quality flag used in our study is described in Table 2.

To incorporate quality flag information in the analysis, we convert a 16-bit integer to a binary value. For instance, the number 196 can be expressed as 000000011000100, which implies the features of bit 2, bit 6, and bit 7 are contained. According to Table 2, pixels with an algorithmic quality flag of 196 are likely to have features of a smaller AOD value than -0.05 or a larger value than 3.6. In addition, it may have a smaller SSA value than 0.82 or larger than 1.0 in the presence of clouds and solar zenith angle being above the threshold or viewing zenith angle being above the threshold. Table 3 provides further details about the quality flags.

Table 2. Quality flags information.

Bits	Definition	Note	Description
0	Reliable	Good	(0, Good; 1: have issue) AOD >0.2 & ALH AK >0.2
1	Less Reliable	Suspect	AOD <0.2 or ALH AK >0.2
2	Out of bounds SSA or AOD at 443 nm.	Bad	AOD <-0.05 or AOD >3.6 or SSA <0.82 or SSA >1.0
3	OE fitting error	Bad	Fitting error during optimal estimation
4	Normalized radiance above threshold	Bad	High normalized radiance
5	Surface albedo above threshold	Bad	High surface albedo
6	Cloud masking	Cloud	Presence of clouds
7	Solar zenith angle above threshold (69°) or viewing zenith angle above threshold	Bad	SZA >69° or VZA >69°
8	Sun-glint angle below threshold over water	Bad	Sun glint angle <35°
9	Terrain height high	Suspect	Terrain height >35°
10	Previous L2 SFC (-5 day) are used	Suspect	Absence of L2 SFC information
11	OMI climatology used for surface albedo	Suspect	Absence of L2 SFC information
12	Previous irradiance used	Suspect	Absence of L1C irradiance
13	AMI cloud-masking used	Cloud	Cloud masking using AMI L2 Cloud product
14	Less reliable of surface albedo	Suspect	Less accurate AERAOD surface albedo
15	Interpolated radiance used	Suspect	LIC Radiance QF=2

Table 3. Process of converting algorithm quality flag 196 into 16-bit unsigned integers to binary. The first equation shows that the decimal number 196 can be summed as $196 = 2^7 + 2^6 + 2^2$, which indicates that it can be converted to the binary number 000000011000100 as written in the second line. To show which bit has the issue based on the converted binary number, we enumerate the bit 0 to bit 16 on the third line. The process shows that bit 2, bit 6, and bit 7 have an issue.

196 =									2^7	2^6				2^2		
196 =	0	0	0	0	0	0	0	0	1	1	0	0	0	1	0	0
bit =	15	14	13	12	11	10	9	8	7	6	5	4	3	2	1	0

Then, we define an uncertainty metric u_i corresponding to a weight λ_i used in the IDW method. The calculation of uncertainty metric, denoted as u_i, is based on a quality flag that is represented by a 16-bit unsigned integer. As mentioned, this integer is first converted into binary format. We then add all the problematic bits with a value of 1 to compute u_i. With this quality flag information, the IDW weight used for our method is

$$\lambda_i = \frac{1/d_i^p u_i^q}{\sum_i 1/d_i^p u_i^q}, \tag{3}$$

where $u_i = \sum(\text{bit values of the qualify flag}) + 1$. Since the high values of u_i imply the low quality of the data, we take the inverse of u_i in the weights of the IDW algorithm. In ~~Equation~~ Eq. (3), q is a power parameter that controls the amount

of quality flag information. The larger the q value, the higher penalty will be assigned to the grid with a large u_i value. In Section 4, we observe that incorporating quality flags in the weight can improve the accuracy of the IDW method. Furthermore, we validate the choice of quality flags from the simulation study.

3.2 Spatio-temporal Merging Algorithm

140 In this section, we describe a merging algorithm (Kikuchi et al., 2018) that can account for spatio-temporal variability in L3 AOD products. By using spatio-temporal information, we can adjust the weights to produce a more robust and accurate L3 AOD mean field output.

3.2.1 Spatio-temporal Variability of AOD_{IDW}

It is crucial to consider the spatio-temporal variability of the IDW estimates when we compute the mean field of L3 AOD

145 products (Kikuchi et al., 2018). However, we only have a single IDW estimate, $AOD_{IDW}(x, y, t)$ at a specific location and time. Since we do not have repeated measures of $AOD_{IDW}(x, y, t)$, the spatio-temporal variability should be computed using neighboring information. Let (x_0, y_0, t_0) be the location and time of interest and (x_i, y_i, t_i) be its neighboring location i. Then spatio-temporal variability is defined as a root-mean-square difference (RMSD) of AOD_{IDW} estimates as

$$\sigma_{IDW}(x_0, y_0, t_0) = \sqrt{\frac{1}{N} \sum_i^N (AOD_{IDW}(x_i, y_i, t_i) - AOD_{IDW}(x_0, y_0, t_0))^2} \tag{4}$$

150 where N is the number of neighboring pixels within ~~the radius of r and~~ r, the distance between the point of interest and its neighboring set and previous T time from (x_0, y_0, t_0). In this work, we consider the ~~radius of four grid lengths~~ fourth-order neighboring grids and window size of $T = 3$ so that $r = 0.1°, 0.2°, 0.3°, 0.4°$ and $t = 0, 1, 2, 3$.

3.2.2 Hourly Merged AOD Estimates

Using the spatio-temporal variability in Section 3.2.1, we computed hourly combined AOD products. The procedure is sum-

155 marized as follows. First, we obtain AOD_{pure} by filtering out unreliable grid points. Then, we compute AOD_{merged} at the location of interest by interpolating AOD_{pure}. From this, we can retrieve reliable AOD products.

Computing AOD_{est}

We first introduce $AOD_{est}(x_0, y_0, t_0)$, which is a weighted average of the IDW estimates obtained in Section 3.1. The AOD estimate at a target grid (x_0, y_0, t_0) is

160
$$AOD_{est}(x_0, y_0, t_0) = \sum_i^n w_i AOD_{IDW}(x_i, y_i, t_0), \tag{5}$$

where

$$w_i = \frac{\frac{1}{\sigma_{IDW}^2(x_i, y_i, t_0)}}{\frac{1}{\sigma_{est}^2(x_i, y_i, t_0)}} \quad \text{and} \quad \frac{1}{\sigma_{est}^2(x_0, y_0, t_0)} = \sum_i^n \frac{1}{\sigma_{IDW}^2(x_i, y_i, t_0)}. \tag{6}$$

Here, n denotes the number of effective pixels within the ~~spatial radius~~ r and past T time from (x_0, y_0, t_0), whose AOD_{IDW} values are greater than equal to 0. In ~~Equation~~ Eq. (5), AOD_{est} is the weighted average of AOD_{IDW} and weights are defined by the inverse of the spatio-temporal variability in Section 3.~~2.~~2.1. Note that the inverse of the variability quantifies the accuracy and reliability of the IDW estimate at each grid; w_i implies the sum of accuracies over the neighboring region of the target point.

Estimating the Error Variance

Our goal is to filter out grid points with high variability. Note that the spatio-temporal variability in ~~Equation (4) becomes small as the spatial or temporal~~ Eq. (4) patio-temporal variability increases as the distance between grids ~~becomes larger~~increases. Utilizing this relationship, we estimate spatial and temporal variability separately through a regression model. The combined variability, denoted as σ_0, at the currently considered grid point (x_0, y_0, t_0) is then calculated as the mean of the spatial and temporal variabilities.

Before estimating the variability, we categorize the value of AOD_{IDW} with different classes. This is because the pattern of spatio-temporal variability varies depending on the magnitude of AOD values (Kikuchi et al., 2018). Specifically, we categorize AOD_{IDW} values into 6 bins of 0.1, 0.25, 0.5, 0.75, 0.9, and 1.0. Note that the previous work (Kikuchi et al., 2018) used 12 number of classes. On the other hand, we use 6 classes because certain classes are rarely observed; using 12 classes can lead to unreliable computation.

Let $\sigma_{dist}(x_0, y_0, t_0)$ be the spatial variability and $\sigma_{time}(x_0, y_0, t_0)$ be the temporal variability of the IDW estimate at (x_0, y_0, t_0). We first compute the average of spatio-temporal variability $\sigma_{IDW}(x_i, y_i, t_i)$ by ~~radius~~ r and class. Then we regress the averaged values obtained for each component of the ~~radius vector ,~~ vector $r = (0.1°, 0.2°, 0.3°, 0.4°)$ ~~,~~ on a design matrix $[1, r, r^2]$, which is a second-order design matrix of ~~radius~~ r for each class. Lastly, we obtain a spatial variability $\sigma_{dist}(x_0, y_0, t_0)$ from the intercept estimate of the quadratic regression model fitting. We can obtain a temporal variability $\sigma_{time}(x_0, y_0, t_0)$ in the similar manner. We first compute the average of spatio-temporal variability $\sigma_{IDW}(x_i, y_i, t_i)$ by time point and class. We regress them on a design matrix $[1, t, t^2]$ for each class and obtain $\sigma_{time}(x_0, y_0, t_0)$ from the intercept estimate of the quadratic regression model fitting.

Finally, we compute the error variance by taking the average of σ_{dist} and σ_{time} as

$$\sigma_0(x_0, y_0, t_0) = \frac{\sigma_{dist}(x_0, y_0, t_0) + \sigma_{time}(x_0, y_0, t_0)}{2}. \tag{7}$$

The calculated error variance contains measurement error caused by sensor noise that varies over time and space shift.

Computing AOD_{pure}

Here, we obtain AOD_{pure} by filtering out uncertain AOD_{IDW} values. For this, we introduce the estimated error of AOD_{pure}, which is defined as

$$\sigma_{pure}(x_0, y_0, t_0) = \begin{cases} \sqrt{\sigma_0^2(x_0, y_0, t_0) + \sigma_{est}^2(x_0, y_0, t_0)}, & \text{if } AOD_{IDW}(x_0, y_0, t_0) \text{ is observed,} \\ \text{missing,} & \text{otherwise.} \end{cases}$$

Here, σ_{est}^2 is the error variance of AOD_{est} from ~~Equation~~Eq. (6) and σ_0^2 is the combined error variance from ~~Equation~~Eq. (7). To filter out uncertain AOD_{IDW} values, we consider an upper threshold of AOD_{IDW} as

$$AOD_{pure}(x_0, y_0, t_0) = \begin{cases} AOD_{IDW}(x_0, y_0, t_0), & \text{if } AOD_{IDW}(x_0, y_0, t_0) \leq AOD_{est}(x_0, y_0, t_0) + 2.58\sigma_{pure}(x_0, y_0, t_0), \\ \text{missing,} & \text{otherwise.} \end{cases} \quad (8)$$

Assuming Gaussian distribution, if $AOD_{IDW}(x_0, y_0, t_0)$ exceeds the upper threshold of the 99% confidence interval, we consider the value is not reliable and exclude it from the mean field calculation.

Computing AOD_{merged}

Based on section 3.2.1, we calculate the total variability within the neighbor grids of the target grid. Then, we use the ratio of the inverse of this total variability as weights to calculate a weighted average for AOD_{pure}, resulting in AOD_{merged} as follows:

$$AOD_{merged}(x_0, y_0, t_0) = \begin{cases} \sum_i^n w_i AOD_{pure}(x_i, y_i, t_0), & \text{if } AOD_{IDW}(x_0, y_0, t_0) \text{ is observed,} \\ \text{missing,} & \text{otherwise,} \end{cases} \quad (9)$$

where

$$w_i = \frac{\frac{1}{\sigma_{pure}^2(x_i, y_i, t_0)}}{\frac{1}{\sigma_{merged}^2(x_0, y_0, t_0)}} \quad \text{and} \quad \frac{1}{\sigma_{merged}^2(x_0, y_0, t_0)} = \sum_i^n \frac{1}{\sigma_{pure}^2(x_i, y_i, t_0)}.$$

This merging process not only utilizes the reliable value AOD_{pure} but also incorporates the reliability σ_{pure} as a weight, resulting in a more trustworthy gap-filling outcome. In fact, in the study by Kikuchi et al. (2018), the ~~RMSE~~ root mean squared error (RMSE) of AOD_{merged} was notably lower at 0.11 compared to the RMSE of 0.20 for AOD_{IDW}.

4 Simulation

4.1 ~~Generating Simulation Data~~

In this section, we conduct a simulation study to validate the choice of quality flags. The data generation procedure is summarized as follows.

4.1 Generating Simulation Data

1. ~~We generate an~~ For our simulation study, we constructed a 70×70 lattice over a 1×1 square domain, with a grid spacing of $0.1°$. Each grid within this lattice represents a location in our simulated dataset. In total, the lattice comprises 4,900 grid cells, covering an area of $7° \times 7°$. Consequently, each unit grid on the lattice represents an area of $0.1° \times 0.1°$. We generate each element of $\mathbf{X} \in \mathbb{R}^{4900 \times 2}$ from ~~$U(0,1)$ and use $\boldsymbol{\beta} = (1,1)$~~ $\text{Unif}(0,1)$ (i.e. the uniform distribution with support [0,1]). This means that we have 4900 locations, each containing two pieces of coordinates information: longitude and latitude. We use $\boldsymbol{\beta}_{1 \times 2} = (1,1)$ as a true coefficient ~~value~~ vector.

2. ~~We create a 70×70 lattice over the $[0,1]^2$ domain and regard each grid as an observed location of the dataset. Then~~ For each location, we simulate zero-mean Gaussian process $\boldsymbol{W}$ from $N(0, (\tau \mathbf{M}' \mathbf{QM})^{-1})$ where $\mathbf{M}$ is obtained by taking the first ~~k~~ k eigenvectors of the Moran operator (Hughes and Haran, 2013) with smoothness parameter τ. Here, $\mathbf{Q} = \text{diag}(\mathbf{A1})$ - $\mathbf{A}$ is a precision matrix calculated from the adjacency matrix, $\mathbf{A}$. Note that $\mathbf{1}$ is all-ones vector.

3. We simulate AOD datasets from $\boldsymbol{Y} = \boldsymbol{X}\boldsymbol{\beta} + \boldsymbol{W} \in \mathbb{R}^{4900 \times 2}$. In our simulation, $\boldsymbol{X}\boldsymbol{\beta}$ represents the fixed effect, while $\boldsymbol{W} \in \mathbb{R}^{4900}$ ~~can~~ account for spatial correlation in AOD products.

4. ~~We~~ To generate missing data for the simulated $\boldsymbol{Y}$ ~~as in~~ that resemble the GEMS L2 product~~. For realistic simulation~~, we apply the observed missing pattern ~~in~~ from the GEMS AOD data to the simulated $\boldsymbol{Y}$ ~~in~~ from Step 3. Specifically, we ~~use the missing pattern of 440nm observed~~ apply the missing data pattern observed in the GEMS AOD data for the $7° \times 7°$ region in East Asia, with a grid spacing of $0.1°$, collected on April 1st at 04:~~45 in the partial area of East Asia, which contains about~~ 45. This selected dataset aligns with a 70×70 lattice in our simulation and contains approximately 20% ~~of missing values~~ missing values, effectively replicating the realistic missing data characteristics found in the actual GEMS AOD observations.

5. For a realistic simulation that incorporates the physical implications of quality flags, we adapt the observed quality flags from the GEMS AOD data to the simulated $\boldsymbol{Y}$ from Step 3. Similar to Step 4, we use the quality flag of the same data (i.e., $7° \times 7°$ (with a unit $0.1°$) in East Asia, observed on April 1st at 04:45) for the simulated $\boldsymbol{Y}$.

We repeat Steps 1 - 3 for 100 times to generate different realizations of $\boldsymbol{Y}$. Then, for each simulated $\boldsymbol{Y}$, we apply the identical missing patterns (Step 4) and quality flags (Step 5) obtained from the real dataset. Figure 2 illustrates an example of a simulated dataset.

4.2 Sensitivity Analysis of q

Here, we investigate the performance of the IDW method on GEMS data by varying q in ~~Equation~~ Eq. (3). Specifically, we consider $q = 0.5, 1$, and 1.5 in our experiment. We first examine whether there is a significant difference in IDW estimates with difference choices of q. Figure 3 indicates that the IDW estimates are comparable with different q values. Table 4 also shows

(a) Simulated AOD values   (b) Missing patterns
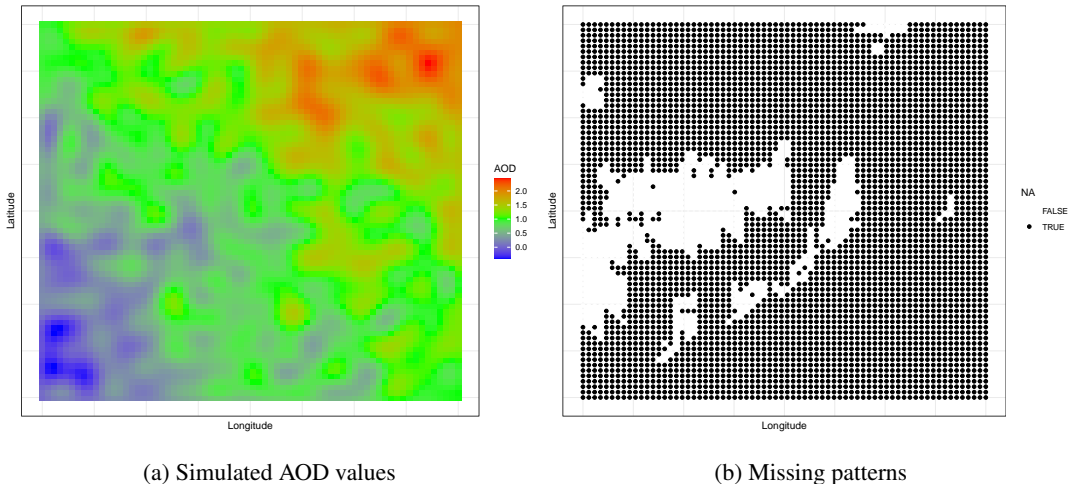
Figure 2. The left figure illustrates the simulated AOD dataset and the right figure shows the missing pattern (white color).
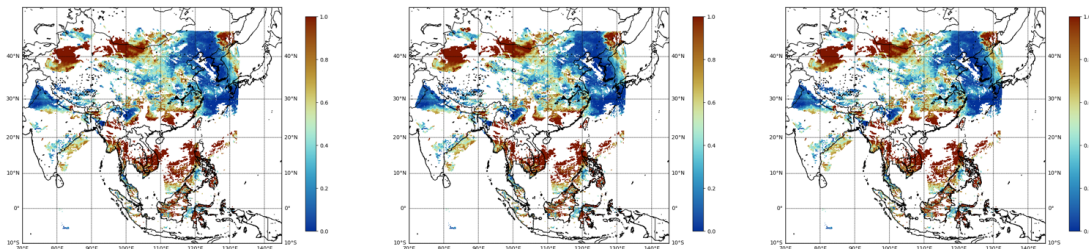
Figure 3. Comparison of the IDW estimates on April 1, 2023, at 7:00 am. Each figure illustrates AOD_{IDW} with $q = 0.5$ (left), $q = 1$ (middle), and $q = 2$ (right).

that the summary statistics of AOD_{IDW} are quantitatively similar with different q choices. Therefore, we conclude that the IDW algorithm is robust to the choice of q. To simplify the calculation, we set $q = 1$ in our analysis.

245   **4.3 Quality Flag Simulation**

As explained in section 4.2 and ~~Equation~~ Eq. (3), quality flag indicators weigh the uncertainty of the IDW algorithm. To improve the accuracy of the IDW algorithm, it is necessary to find the optimal bit combination of the quality flag by performing simulation studies. Therefore, we first discover bits that show substantially lower ~~MSE~~mean squared error (MSE), then combine such particular bits into groups. Here, MSE is calculated between the simulated AOD dataset and IDW results, which is given as

$$\frac{1}{n}\sum_{i=1}^{n}(AOD_i - IDW_i)^2$$

where AOD_i is the simulated AOD values on location i and IDW_i is the IDW result on location i. Note that we refer to these bit combinations of the quality flags as a "case." For example, we may discover bit 0,1,2 has a significantly low MSE. Then we can create various combinations that include 0,1,2 such as $0 \cdot 1$, $0 \cdot 2$, or even $0 \cdot 1 \cdot 2$, and each can be denoted as a particular "case".

Table 4. Summary statistics of AOD_{IDW} values with different q values on April 1, 2023, at 7:00 am.

Exponent (q)	Mean	Standard deviation	Min	25% quantile	Median	75% quantile	Max
$q = 0.5$	0.6139	0.5534	0.0	0.2003	0.4895	0.8654	3.5928
$q = 1$	0.6121	0.5539	0.0	0.1966	0.4876	0.8642	3.5928
$q = 2$	0.6173	0.5524	0.0	0.2081	0.4935	0.8673	3.5928
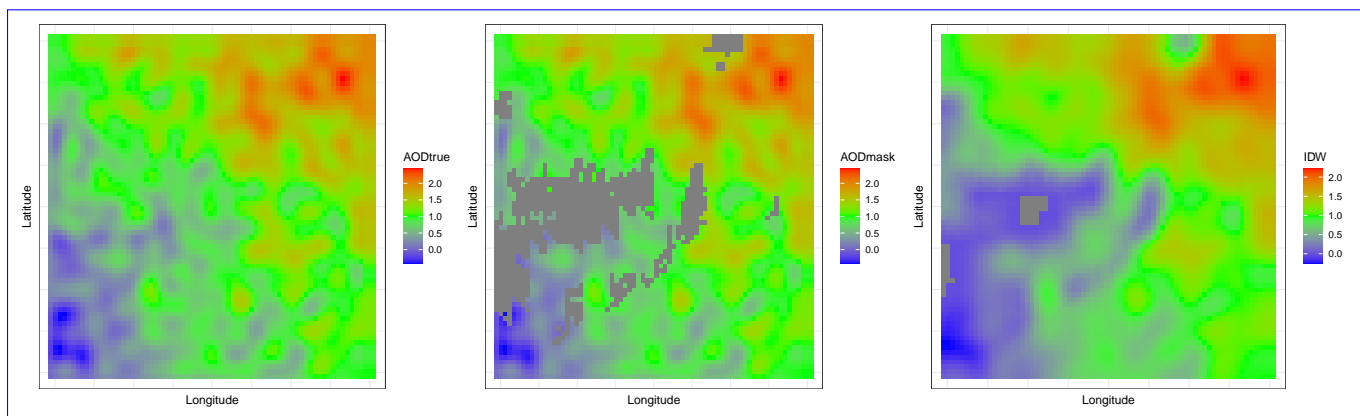
Figure 4. The left figure shows the simulated AOD values while the middle figure shows the simulated data incorporated with the missing pattern, which can be distinguished by the gray color. The right figure illustrates the result of applying the IDW algorithm to simulated data with ~~radius 9.~~ $r = 3$.

Before finding an optimal case of the quality flag through a simulation study, we examine whether the result differs depending on the ~~radius of~~ value of r in the IDW algorithm~~r~~. Note that this simulation study defines the unit of r ~~radius~~ as one unit grid, not the distance based on coordinates as described in 3.1. ~~We fixed the radius as 9 since varying the radius size did not show any notable difference in MSE, yet it shows a better imputation of the IDW algorithm as described~~ After careful consideration and analysis, we have chosen to set the neighboring order to 3 for our study because varying the order of neighbor did not yield any significant differences in the mean squared error (MSE). However, to provide a comprehensive understanding of the impact of order on the interpolation process, we have included additional IDW results with increasing order sizes in Appendix A. These supplementary results demonstrate that larger order sizes can potentially lead to oversmoothing. Figure 4 shows the generated AOD simulation data, where the center figure is the data applying the missing value pattern, and the right figure is the visualization result showing the result of applying the IDW algorithm to the data.

260   We then follow the following procedure. After selecting particular bits with lower MSE than others fixed with ~~radius 9~~order of 3, we repeat the experiment to reflect diverse uncertainty term calculations by considering various cases in the IDW algorithm. We then find the optimal case that obtains the highest accuracy after comparing the accuracies between the cases. Here, MSE values are evaluated between the simulation and the imputed data after regarding the simulated data as real data.
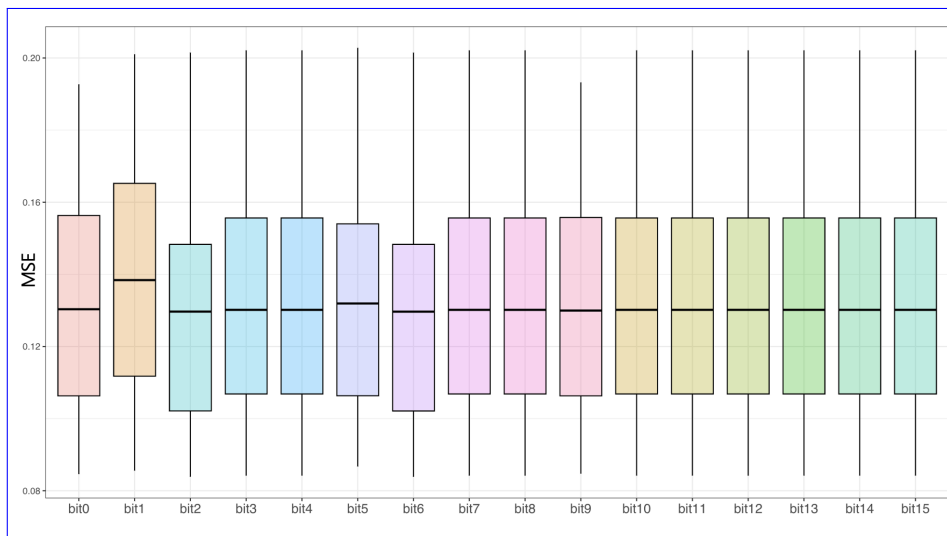
Figure 5. Boxplot with interquartile range describing the IDW algorithm results on 100 repetitive simulation datasets, including bit 0 to bit 15 respectively in uncertainty metric $\sigma(i)$. The boxes represent the interquartile range since they are drawn from Q1 to Q3, with a horizontal line drawn inside to denote the median of the repeated simulations. The boundary of the lower whisker is the minimum value of the MSE. In contrast, the boundary of the upper whisker is the maximum value of the MSE among repeated simulations. We discover that bit 2 and bit 6 have lower MSE compared to other bits.

    To select the quality flag bit for making the combination case, we first calculate the MSE for every quality flag bit. Figure 5
265 expresses the MSE value as a boxplot for every bit. Although each consecutive boxplot indicates the result of bit 0 to 15, bit 2 and bit 6 have significantly lower MSEs than others. The medians for each bit are 0.122 and 0.123, respectively. Bit 2 defines whether SSA or AOD is out of a specific value range, while bit 6 shows the presence of clouds. We then compose six various candidate cases, including bit 2 and bit 6. Table 5 summarized six various candidate cases.

    To find the optimal quality control case that yields the lowest MSE among six candidate cases, we calculate the MSE for
270 each case with two different τ, $\tau = 1$ and $\tau = 6$, and draw boxplots in 6. From Figure 6(a) and Figure 6(b), each case shows a different MSE, while Case 5, which contains bit 0, 2, and 6, shows the lowest median of 0.387 in Figure 6(a). Therefore, in our real application, we use the quality flag to Case 5 (bit 0, 2, and 6) when calculating the uncertainty term for the IDW algorithm.

    We check whether the optimal case for IDW algorithm changes depending on the smoothing parameter τ of simulation data. Figure 6(a) and Figure 6(b) show the average MSE, which is represented as a box plot as above, with different smoothing

Table 5. Six candidate cases for selecting quality flag with the combinations of bit 0, 2, and 6.

	Case 1	Case 2	Case 3	Case 4	Case 5	Case 6
Bits	All	0	2	6	0,2,6	Nothing
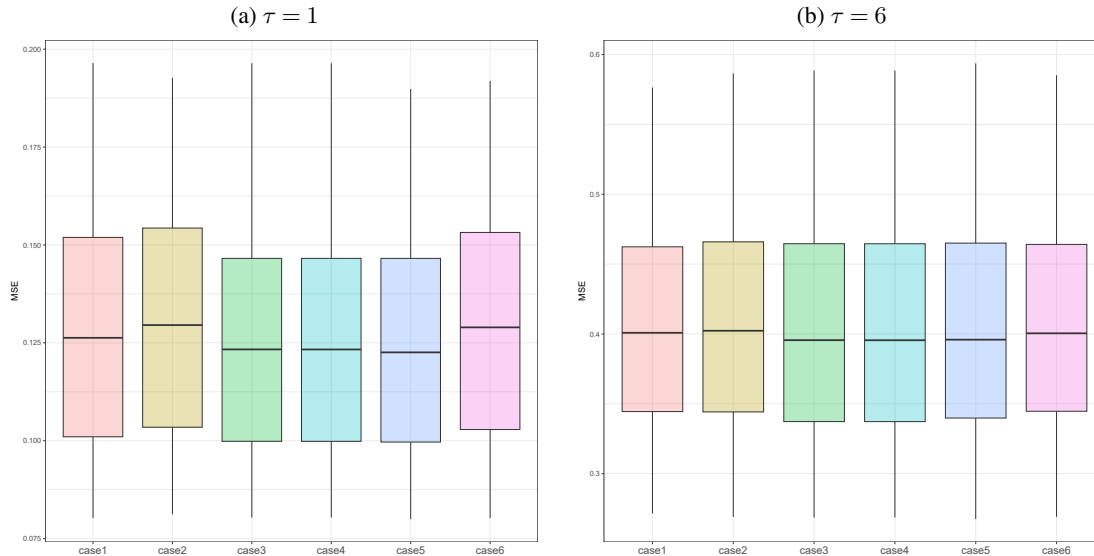
Figure 6. The left figure shows the simulation results with $\tau = 1$ while the right figure shows the results with $\tau = 6$. Despite the value of smoothing parameter τ, we discover that the hierarchy of the MSE values between the cases are identical.

parameters. We discover that the overall magnitude of the MSE value remains different, but the hierarchy of the MSEs across the cases is unchanged. It implies that the algorithm's performance is robust regardless of the smoothing parameter.

5 GEMS Data Application

5.1 Spatial Resolution of Output Product

~~In our study, we set the mean field spatial resolution as $0.1° \times 0.1°$ longitude-latitude grid, which is larger than the grid length of 7 km × 8 km.~~ A geostationary satellite instrument such as GEMS observes a fixed position. Therefore, if we use grids that are too small, the output will have many missing values; an appropriate grid size should be selected in terms of the coverage of the mean fields. Furthermore, we need to consider effective range, accuracy, and computation time to obtain mean fields when we choose a grid size. If we use too fine spatial resolution, computational cost will be exponentially increased. On the other hand, grid sizes that are too large can lead to inaccurate output results. Accordingly, in our study, we set the mean field spatial resolution as $0.1° \times 0.1°$ and $0.05° \times 0.05°$ longitude-latitude grid for the East Asia and Korean Peninsula region, respectively.

5.2 Level 2 Aerosol Optical Depth Data

As evidenced by various studies (Kaufman et al., 2005; Loeb and Manalo-Smith, 2005; Matheson et al., 2005), AOD exhibits a positive correlation with Cloud Fraction (CF), implying that proximity to clouds can result in a statistical increase in AOD measurements. Additionally, a dependency of AOD on solar and viewing zenith angles was observed (de Miguel et al., 2011), highlighting the complexities involved in accurate AOD estimation under varied atmospheric conditions. To address these complexities, this study involved masking data based on ~~quality flags incorporated within the~~ three variables given below. Cloud radiance fraction is incorporated within GEMS L2 cloud product, and the others are incorporated within GEMS AOD L2 product. These ~~quality flags~~ variables are meticulously designed to account for variability and uncertainties in satellite data (Choi et al., 2020), addressing factors such as solar and viewing zenith angles, and cloud radiance fraction. This methodology ensures a more precise and reliable estimation of AOD, which is crucial in understanding atmospheric dynamics and environmental monitoring. The unreliable values are treated as missing values when we apply the IDW algorithm.

- cloud radiance fraction ≥ 0.4,

- solar zenith angle ≥ 70 degrees, and

- viewing zenith angle ≥ 70 degrees

In our study, we set two spatial domains of the mean field outputs, one with latitude (30° N-43° N) and longitude (123° E-131° E) corresponding to the vicinity of the Korean Peninsula and the other with latitude (32° N-43° N) and longitude (115° E-131° E) including the vicinity of the Shandong Peninsula in China.

5.3 Mean Field Estimates of GEMS AOD L3 Product

~~As we described in Section 3, we obtain AOD$_{pure}$ from AOD$_{est}$ by considering both the spatio-temporal variability σ_{est} and the estimation uncertainty σ_{est}. This procedure allows us to obtain more reliable AOD estimates. Furthermore, we can use more robust AOD estimates when we compute the mean field, resulting in smoother output.~~

Figures 7 and 8 compare the spatio-temporal merged products with the simply averaged products. For spatio-temporal merged AOD L3 products, we apply the procedure described in Section 3. On the other hand, we take a mean of the IDW estimates for simply averaged AOD L3 products. As mentioned in Kikuchi et al. (2018), grid points with AOD values exceeding 1.0 are extremely rare. Therefore, to focus on the majority of values for detailed characterization, we set the threshold at 1.0. In Figure 7, we observe that more missing values occur in the area of latitude (20° N-30° N) and longitude (130° E-140° E) for the spatio-temporally merged products compared to the simply averaged products. It can also be checked by the ratio of missing values for each product given in each figure. This is due to the fact that a spatio-temporal merging procedure only considers reliable AOD estimates, while a simple averaging method does not. Therefore, the simply averaged products can be regarded as more unreliable, though they have less number of missing values. In Figure 7, we also observe that the spatio-temporal merging method can provide smoother mean field outputs; for example, there is a significant difference in the area of latitude
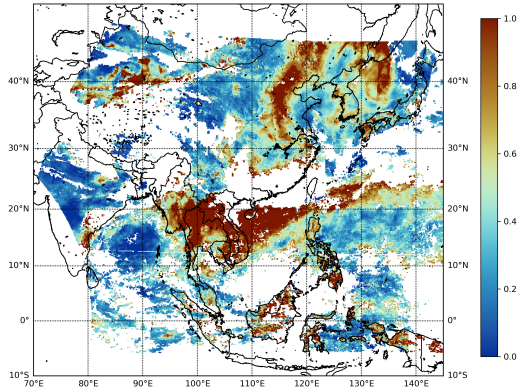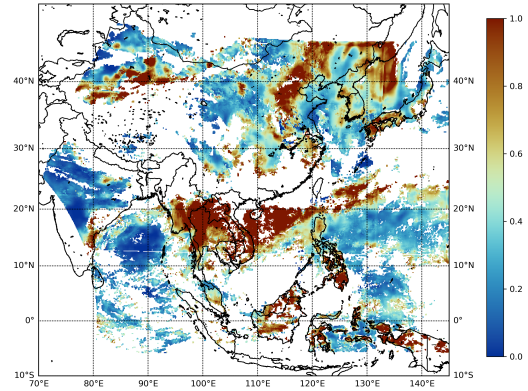
(a) Simply averaged output. (b) Spatio-temporally merged output.

Figure 7. Daily mean-field estimates of GEMS AOD L3 product on April 1, 2023, at the wavelength of ~~354nm~~354 nm. Missing ratio : (a) 0.5031, (b) 0.5733.
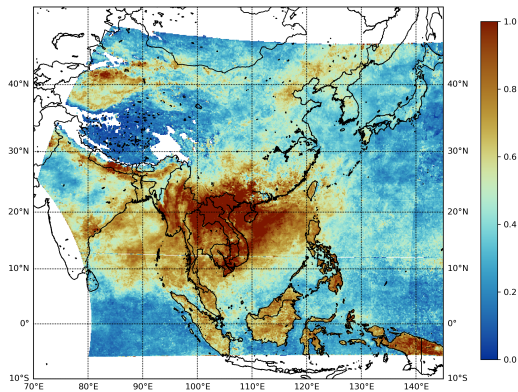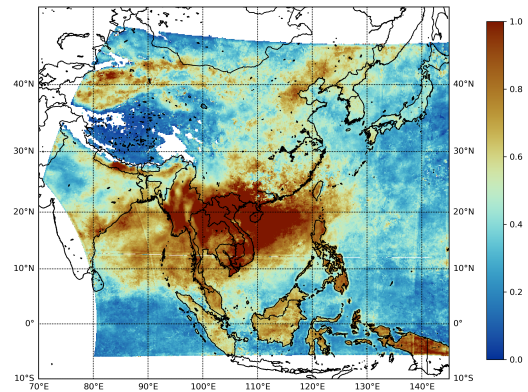
(a) Simply averaged output. (b) Spatio-temporally merged output.

Figure 8. Monthly mean-field estimates of GEMS AOD L3 product in April, 2023, at the wavelength of ~~354nm~~354 nm. Missing ratio : (a) 0.1485, (b) 0.1489.

(35° N-45° N) and longitude (125° E-135° E). Similar trends are also observed in Figure 8. Mean field estimates at all three wavelengths for East Asia and Korea are provided in Appendix B and C, respectively.

As we described in Section 3, we obtain AOD_{pure} from AOD_{est} by considering both the spatio-temporal variability σ_0 and the

320 estimation uncertainty σ_{est}. This procedure allows us to obtain more reliable AOD estimates. Furthermore, we can use more robust AOD estimates when we compute the mean field, resulting in smoother output.

5.4 Qualitative Evaluation for the Mean Field Products

Direct evaluation of the accuracy of the AOD L3 mean field products is challenging because there are no true values for the products. Therefore, we compare our results with previous studies with qualitative aspects.
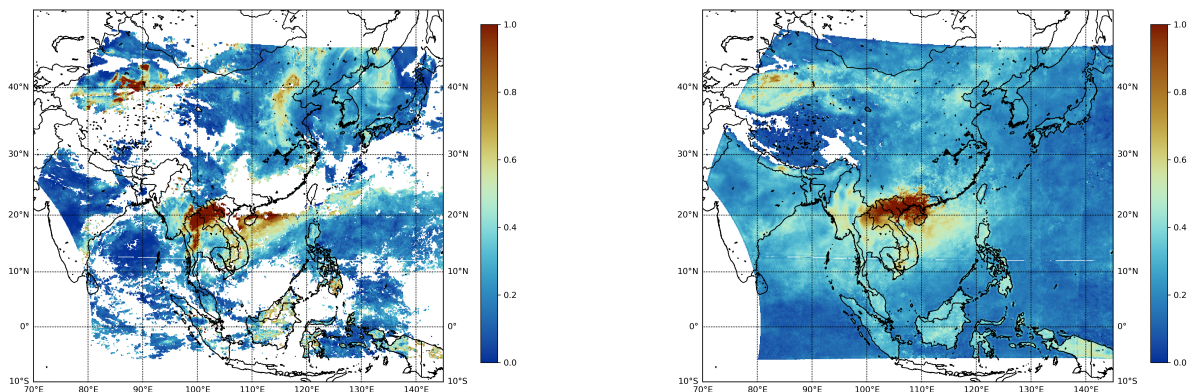
(a) Daily Mean Field Output on April 1, 2023.

(b) Monthly Mean Field Output on April 1, 2023.

Figure 9. Mean-field estimates of GEMS AOD L3 product on April 1, 2023 at the wavelength of ~~550nm~~ 550 nm.

325 In Figure 9 (a), we observe that our mean field products at ~~550nm~~ 550 nm wavelength on April 1 are similar to the springtime global distribution of AOD at the same wavelength. Furthermore, high values are observed near the Taklamakan Desert due to dust and also observed in Southeast Asia during spring due to biomass burning. This indicates that the computed mean fields can effectively capture real-world phenomena. In addition, we observe that overall trends of AOD values are similar to that from ~~MODIS~~ Moderate Resolution Imaging Spectroradiometer (MODIS) data (Tian et al., 2023), though there are some
330 discrepancies in the vicinity of the Taklamakan Desert and certain areas in Southeast Asia.

5.5 Quantitative Evaluation for the Mean Field Products

To measure the smoothness of mean field products, we compute the second-order gradients of the AOD estimates from longitude and latitude. Specifically, we compute gradients at each pixel point from its neighboring AOD values following previous studies (Fornberg, 1988; Quarteroni et al., 2007; Durran, 1999). Then, we compare the absolute mean of the gradients
335 from the simple and spatio-temporal averaging methods. Table 6 indicates that gradients from both directions are smaller in

the spatio-temporally merging method. Considering that AOD exhibits significant spatio-temporal variability, our method can provide more realistic mean field products than the simple averaging method.

Table 6. Comparison of gradients between merging algorithms

Axis	Simply Averaged Mean Field	Spatio-temporal Merged Mean field
Longitude	0.00481	0.00416
Latitude	0.00488	0.00424
Both	0.00783	0.00685

6   Conclusions

In remote sensing, data have been processed to different ~~units~~levels. For example, the L2 dataset, which contains atmospheric state retrievals, is converted to the L3 dataset. Specifically, we focus on AOD retrievals from the GEMS ~~satellite~~ instrument through gap filling and noise filtering. We improve the quality of L3 AOD mean field products by considering quality flag information and spatio-temporal variability (Kikuchi et al., 2018). Specifically, the contribution of our work is summarized as follows.

First, we improve the performance of the IDW algorithm by including quality flag information in the weight calculation. We assign weights inversely proportional to the number of poor quality indicators. To validate the choice of different quality flags, we conduct simulation studies. We observe that including bits 0, 2, and 6 from the quality flags significantly improves the accuracy of the IDW algorithm. We apply this novel approach to GEMS ~~ADO~~ AOD data covering various regions and wavelengths.

Second, we apply spatio-temporal merging method (Kikuchi et al., 2018) to GEMS AOD data. Compared to the previous work (Park et al., 2023) that only considers spatial variability, our method can also account for temporal variability from the previous time points. We observe that our mean field products show a similar trend to the previous studies, indicating that the products are reliable.

Although our current study has made notable progress in enhancing the accuracy of AOD mean field estimation, several avenues for future research remain open. One potential direction involves integrating additional data, such as cloud information and the distinction between oceanic and terrestrial regions, which could further refine our results by considering the impact of cloud cover on aerosol retrievals. ~~Additionally, validating~~ Our method can account for variability due to cloud contamination by utilizing quality flag information in the IDW estimates. Note that we cannot use physical mechanisms (e.g., aerosols produced from a wildfire) in the interpolation step due to the limited data sources. Developing extensions of our approach by incorporating physical mechanisms may provide interesting future research avenues. Additionally, with the available information on quality flags, one direction for future work is to develop methodologies for adaptively weighting or selecting quality flag bits by employing statistical variable selection methodologies. Validating our AOD mean field products against ground-based measurements or other satellite datasets could also offer valuable insights into their reliability and

consistency, thereby helping to identify any potential biases or uncertainties. Lastly, sensitivity analysis for the choice of hyper-parameters (e.g., ~~radius~~order of neighboring grids, time windows) would be useful to improve the performance of the method.

365   *Data availability.*   The GEMS Level 2 products are available at https://nesc.nier.go.kr/ko/html/index.do (last access: 28 February 2024)

Appendix A: Sensitivity Analysis for the Raidus of the IDW Algorithm

We compare the IDW algorithm application result varying the ~~radius r~~order of neighboring grids used for weighted average. We find a remarkable difference in the imputed area viewed in the visualization as fewer missing values remain when the ~~$r = 9$~~order 9 compared to the ~~$r = 3$.~~order 3. However, each MSE value is 0.255 and 0.25, respectively, showing no significant
370   difference in numbers. Even with a negligible difference between the two window sizes, we determined that the window size should be ~~9 since it covers more missing areas and has a lower MSE value~~3 since order of 9 could cause oversmoothing.
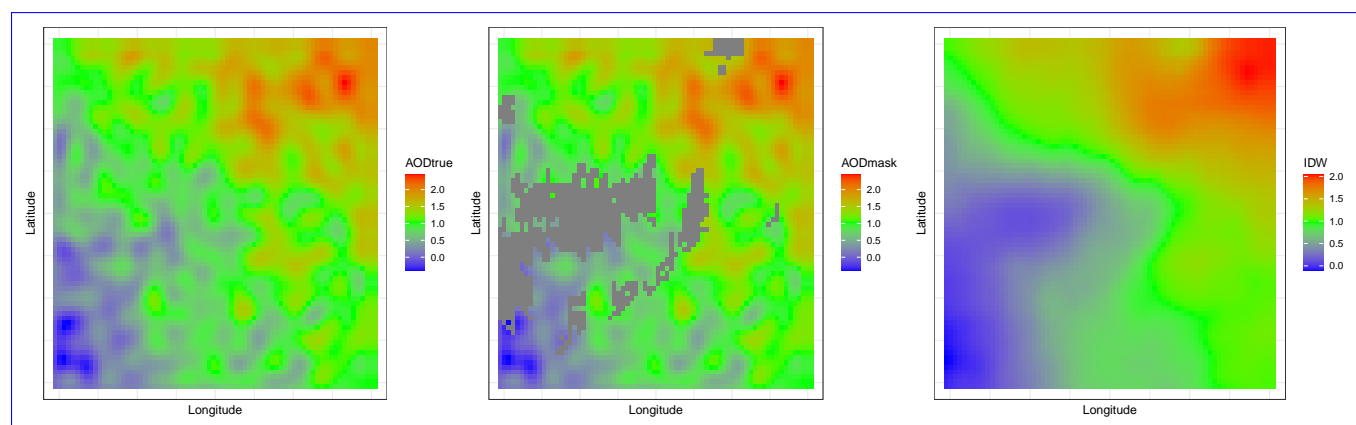
Figure A1. The left figure shows the simulated AOD values while the middle figure shows the simulated data incorporated with the missing pattern, which can be distinguished by the gray color. The right figure illustrates the result of applying the IDW algorithm to simulated data with ~~radius 3.~~order 9.

Appendix B: Mean Field Estimates of GEMS AOD L3 Product for East Asia

In this section, we include daily and monthly mean-field estimates of GEMS AOD L3 products at all three wavelengths for East Asia.
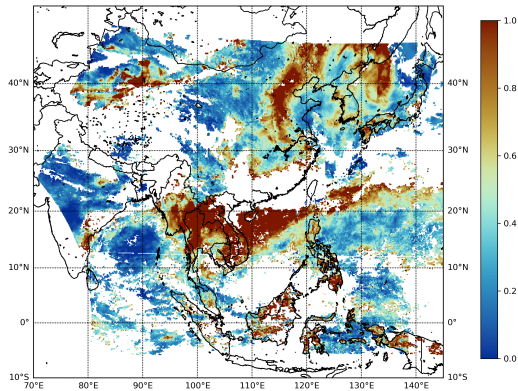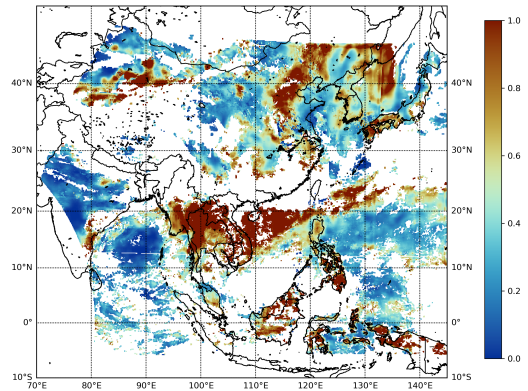
(a) Simply averaged output.   (b) Spatio-temporally merged output.

Figure B1. Daily mean-field estimates of GEMS AOD L3 product on April 1, 2023, at the wavelength of ~~354nm~~354 nm. Missing ratio : (a) 0.5031, (b) 0.5733.
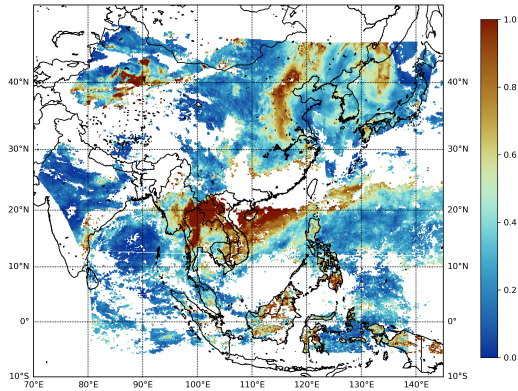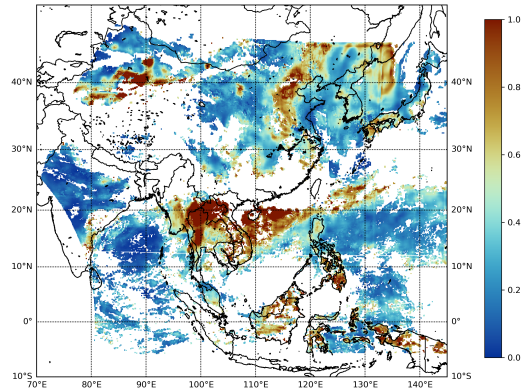
(a) Simply averaged output.   (b) Spatio-temporally merged output.

Figure B2. Daily mean-field estimates of GEMS AOD L3 product on April 1, 2023, at the wavelength of ~~443nm~~443 nm. Missing ratio : (a) 0.5000, (b) 0.5710.
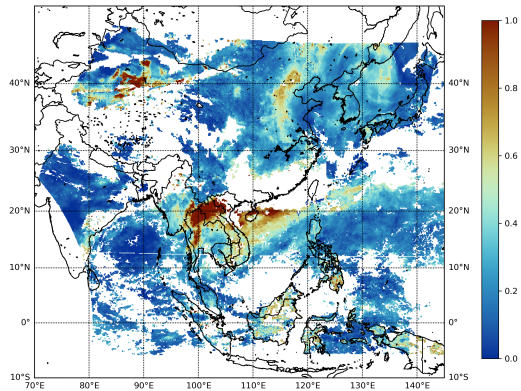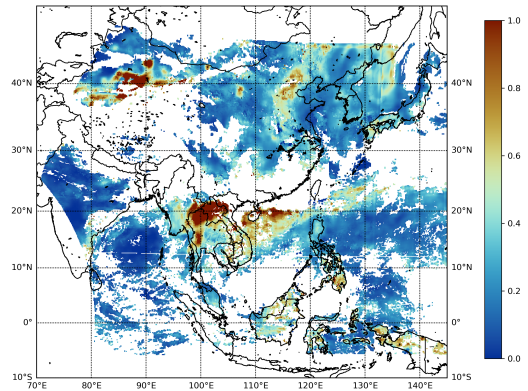
(a) Simply averaged output.   (b) Spatio-temporally merged output.

Figure B3. Daily mean-field estimates of GEMS AOD L3 product on April 1, 2023, at the wavelength of ~~550nm~~550 nm. Missing ratio : (a) 0.4908, (b) 0.5619.
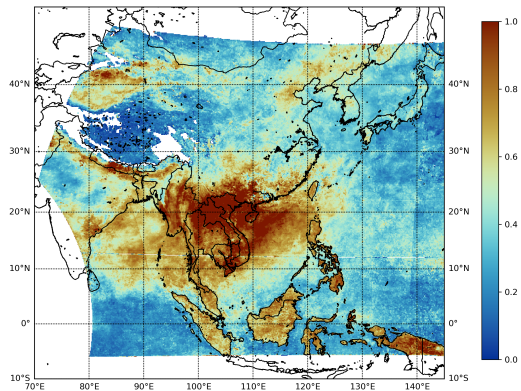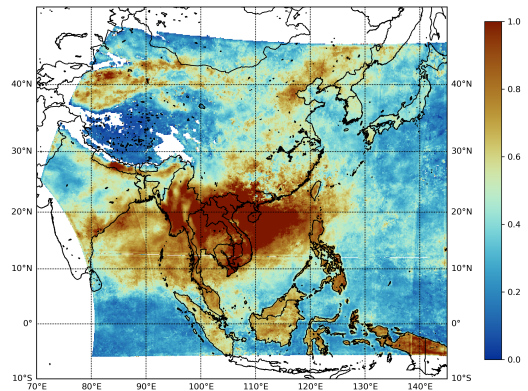
(a) Simply averaged output.   (b) Spatio-temporally merged output.

Figure B4. Monthly mean-field estimates of GEMS AOD L3 product in April, 2023, at the wavelength of ~~354nm~~354 nm. Missing ratio : (a) 0.1485, (b) 0.1489.
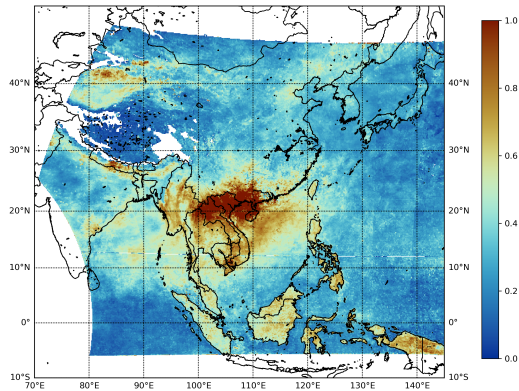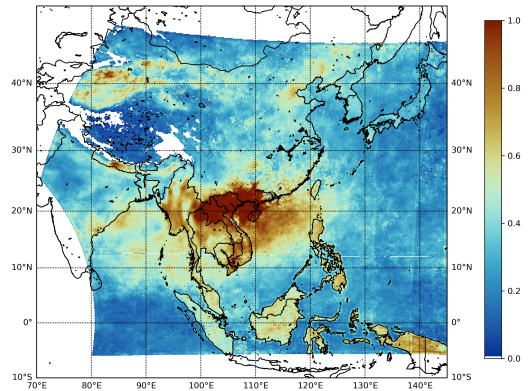
(a) Simply averaged output.   (b) Spatio-temporally merged output.

Figure B5. Monthly mean-field estimates of GEMS AOD L3 product in April, 2023, at the wavelength of ~~443nm~~443 nm. Missing ratio : (a) 0.1490, (b) 0.1494.
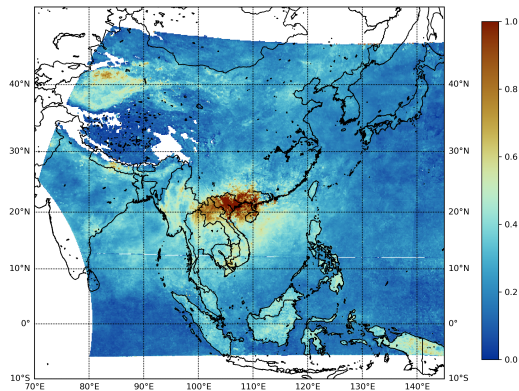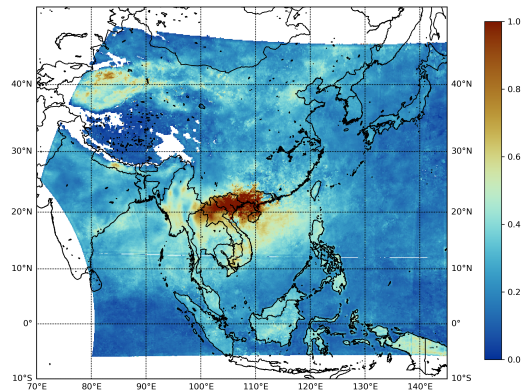
(a) Simply averaged output.   (b) Spatio-temporally merged output.

Figure B6. Monthly mean-field estimates of GEMS AOD L3 product in April, 2023, at the wavelength of ~~550nm~~550 nm. Missing ratio : (a) 0.1483, (b) 0.1487.

 Appendix C: Mean Field Estimates of GEMS AOD L3 Product for Korea

In this section, we include daily and monthly mean-field estimates of GEMS AOD L3 products for three wavelengths for Korea.
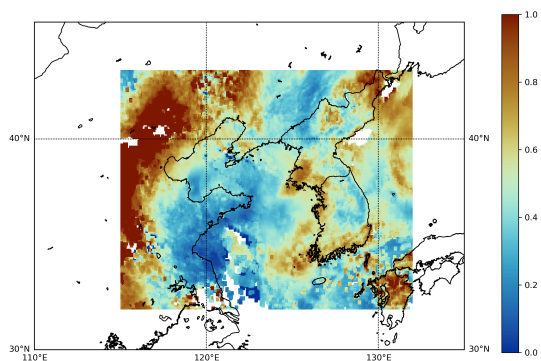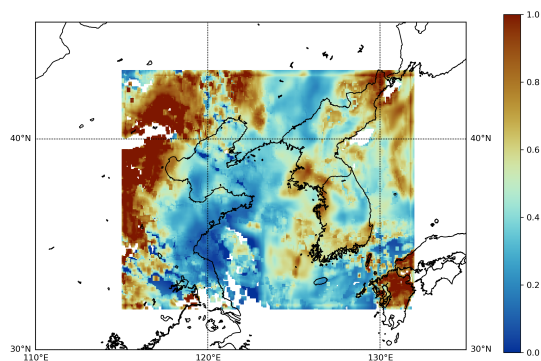
(a) Simply averaged output.   (b) Spatio-temporally merged output.

Figure C1. Daily mean-field estimates of GEMS AOD L3 product on April 1, 2023, at the wavelength of ~~354nm~~354 nm. Missing ratio : (a) 0.0263, (b) 0.0386.
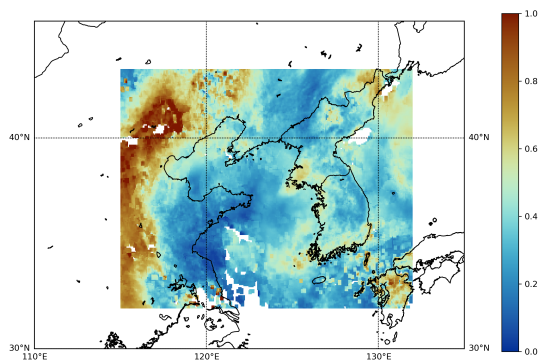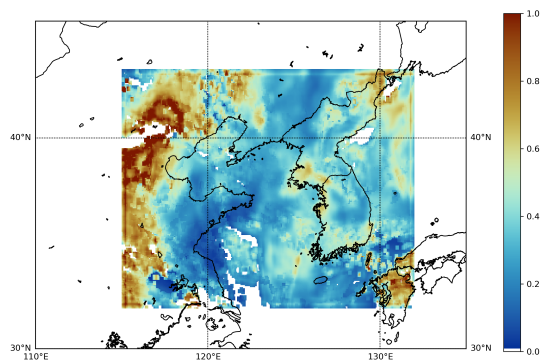
(a) Simply averaged output.   (b) Spatio-temporally merged output.

Figure C2. Daily mean-field estimates of GEMS AOD L3 product on April 1, 2023, at the wavelength of ~~443nm~~443 nm. Missing ratio : (a) 0.0255, (b) 0.0406.
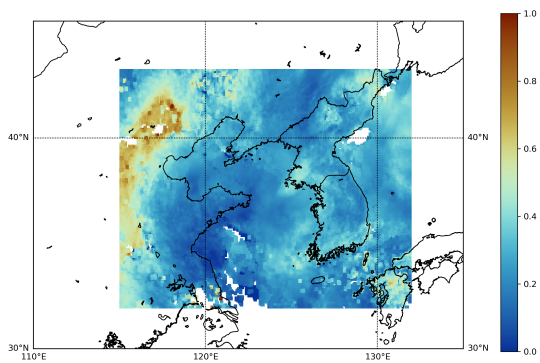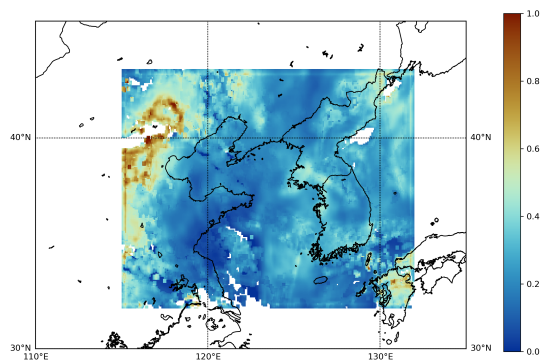
(a) Simply averaged output.   (b) Spatio-temporally merged output.

Figure C3. Daily mean-field estimates of GEMS AOD L3 product on April 1, 2023, at the wavelength of ~~550nm~~550 nm. Missing ratio : (a) 0.0194, (b) 0.0309.
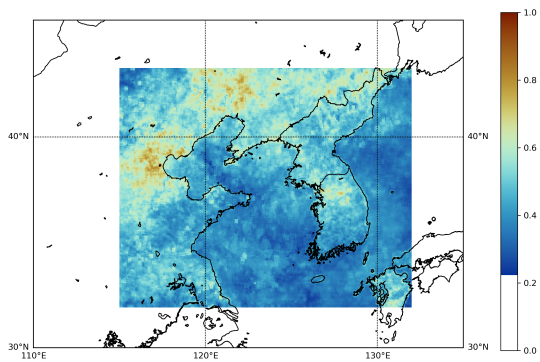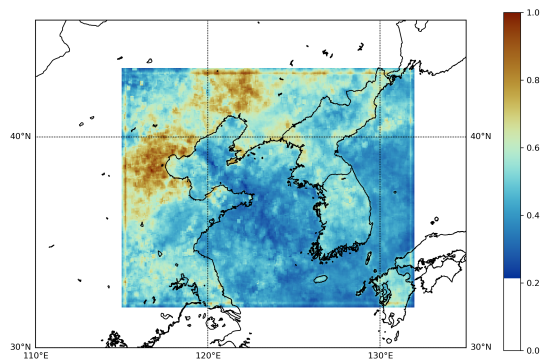
(a) Simply averaged output.   (b) Spatio-temporally merged output.

Figure C4. Monthly mean-field estimates of GEMS AOD L3 product in April, 2023, at the wavelength of ~~354nm~~354 nm. Missing ratio : (a) 0.0, (b) 0.0.
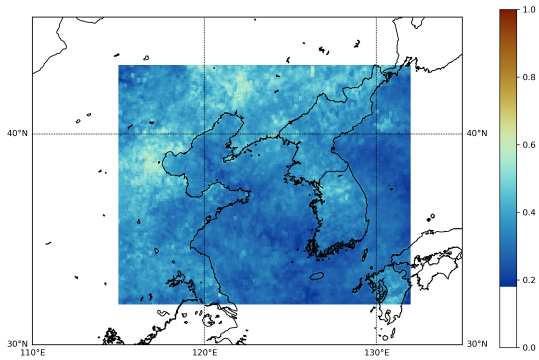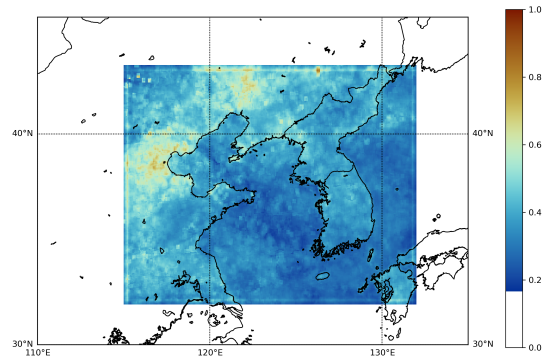
(a) Simply averaged output.   (b) Spatio-temporally merged output.

Figure C5. Monthly mean-field estimates of GEMS AOD L3 product in April, 2023, at the wavelength of ~~443nm~~443 nm. Missing ratio : (a) 0.0, (b) 0.0.
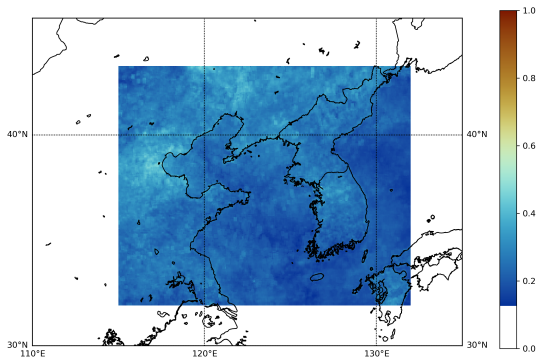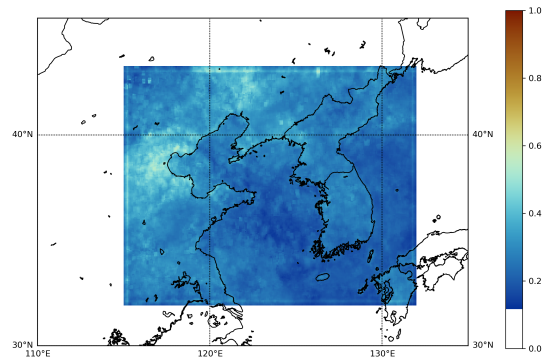
(a) Simply averaged output.   (b) Spatio-temporally merged output.

Figure C6. Monthly mean-field estimates of GEMS AOD L3 product in April, 2023, at the wavelength of ~~550nm~~550 nm. Missing ratio : (a) 0.0, (b) 0.0.

Author contributions. GEMS data were provided by YSC, JK and WK. All authors participated in developing the overall algorithm design based on a conceptual idea of a Spatio-temporal merging algorithm by SK. Specifically, Spatio-temporal merging algorithms were developed by SK and SP with the guidance of JP and IHJ. Simulation studies of quality flags incorporated in Spatio-temporal merging algorithms were conducted by SL and DO. Data analyses were made by YHC and HK. The paper was written, edited, and proofread by all the authors.

380

Competing interests. The contact author has declared that none of the authors has any competing interests.

Acknowledgements. This work was supported by the National Research Foundation of Korea (2020R1C1C1A0100386814, RS-2023-00217705, RS-2023-00218377), ICAN (ICT Challenge and Advanced Network of HRD) support program (RS-2023-00259934) supervised by the IITP (Institute for Information & Communications Technology Planning & Evaluation). The authors are grateful to the anonymous reviewers for their careful reading and valuable comments.

385

References

Abdullah, S., Ismail, M., Ali Najah Ahmed, A.-M., and Abdullah, A.: Forecasting Particulate Matter Concentration Using Linear and Non-Linear Approaches for Air Quality Decision Support, Atmosphere, 10, 667, https://doi.org/10.3390/atmos10110667, 2019.

Alexander, L., Allen, S., Bindoff, N., Breon, F.-M., Church, J., Cubasch, U., Emori, S., Forster, P., Friedlingstein, P., Gillett, N., Gregory, J., Hartmann, D., Jansen, E., Kirtman, B., Knutti, R., Kanikicharla, K., Lemke, P., Marotzke, J., Masson-Delmotte, V., and Xie, S.-P.: Climate change 2013: The physical science basis, in contribution of Working Group I (WGI) to the Fifth Assessment Report (AR5) of the Intergovernmental Panel on Climate Change (IPCC), 2013.

Brauer, M., Freedman, G., Frostad, J., Donkelaar, A., Martin, R., Dentener, F., Van Dingenen, R., Estep, K., Amini, H., Apte, J., Balakrishnan, K., Barregard, L., Broday, D., Feigin, V., Ghosh, S., Hopke, P., Knibbs, L., Kokubo, Y., Liu, Y., and Cohen, A.: Ambient Air Pollution Exposure Estimation for the Global Burden of Disease 2013, Environmental Science & Technology, https://doi.org/10.1021/acs.est.5b03709, 2015.

Charlson, R.: Atmospheric visibility related to aerosol mass concentration - A review, Environmental Science & Technology, 3, https://doi.org/10.1021/es60033a002, 1969.

Charlson, R. J., Schwartz, S. E., Hales, J. M., Cess, R. D., Coakley, J. A., Hansen, J. E., and Hofmann, D. J.: Climate Forcing by Anthropogenic Aerosols, Science, 255, 423–430, https://doi.org/10.1126/science.255.5043.423, 1992.

Chen, C., Dubovik, O., Schuster, G., Chin, M., Henze, D., Lapyonok, T., Derimian, Y., and Ying, Z.: Multi-angular polarimetric remote sensing to pinpoint global aerosol absorption and direct radiative forcing, Nature Communications, 13, https://doi.org/10.1038/s41467-022-35147-y, 2022.

Chen, M. and Tsai, Y. I.: Characterization of visibility and atmospheric aerosols in urban, suburban, and remote areas, The Science of the total environment, 263, 101–14, https://doi.org/10.1016/S0048-9697(00)00670-7, 2001.

Cho, Y., Kim, J., Go, S., Kim, M., Lee, S., Kim, M., Chong, H., Lee, W.-J., Lee, D.-W., Torres, O., and Park, S. S.: First Atmospheric Aerosol Monitoring Results from Geostationary Environment Monitoring Spectrometer (GEMS) over Asia, https://doi.org/10.5194/amt-2023-221, 2023.

Choi, Y.-S., Kim, G., Kim, B.-R., and Kwon, M.-J.: Geostationary Environment Monitoring Spectrometer (GEMS) Algorithm Theoretical Basis Document Cloud Retrieval Algorithm, Atmospheric Measurement Techniques, 1.1, 29, https://nesc.nier.go.kr/ko/html/satellite/doc/doc.do, 2020.

Cressie, N.: Mission CO 2 ntrol: A Statistical Scientist's Role in Remote Sensing of Atmospheric Carbon Dioxide, Journal of the American Statistical Association, 113, 152–168, https://doi.org/10.1080/01621459.2017.1419136, 2018.

de Miguel, A., Mateos, D., Bilbao, J., and Román, R.: Sensitivity analysis of ratio between ultraviolet and total shortwave solar radiation to cloudiness, ozone, aerosols and precipitable water, Atmospheric research, 102, 136–144, 2011.

Durran, D. R.: Numerical methods for wave equations in geophysical fluid dynamics / Dale R. Durran., Texts in applied mathematics, Springer, ISBN 0387983767, 1999.

Fornberg, B.: Generation of Finite Difference Formulas on Arbitrarily Spaced Grids, Mathematics of Computation, 51, 699–706, http://www.jstor.org/stable/2008770, 1988.

Go, S., Kim, J., Mok, J., Irie, H., Yoon, J., Torres, O., Krotkov, N., Labow, G., Kim, M., Koo, J.-H., Choi, M., and Lim, H.: Ground-based retrievals of aerosol column absorption in the UV spectral region and their implications for GEMS measurements, Remote Sensing of Environment, 245, 111 759, https://doi.org/10.1016/j.rse.2020.111759, 2020a.

Go, S., Kim, J., Park, S. S., Kim, M., Lim, H., Kim, J.-Y., Lee, D.-W., and Im, J.: Synergistic Use of Hyperspectral UV-Visible OMI and Broadband Meteorological Imager MODIS Data for a Merged Aerosol Product, Remote Sensing, 12, 3987, https://doi.org/10.3390/rs12233987, 2020b.

Hughes, J. and Haran, M.: Dimension reduction and alleviation of confounding for spatial generalized linear mixed models, Journal of the Royal Statistical Society Series B: Statistical Methodology, 75, 139–159, 2013.

Isaaks, E. H. and Srivastava, R. M.: Applied geostatistics, (No Title), 1989.

Kaufman, Y., Tanré, D., and Boucher, O.: A satellite view of aerosols in the climate system, Nature, 419, 215–23, https://doi.org/10.1038/nature01091, 2002.

Kaufman, Y., Koren, I., Remer, L., Tanré, D., Ginoux, P., and Fan, S.: Dust transport and deposition observed from the Terra-Moderate Resolution Imaging Spectroradiometer (MODIS) spacecraft over the Atlantic Ocean, Journal of Geophysical Research: Atmospheres, 110, 2005.

Kikuchi, M., Murakami, H., Suzuki, K., Nagao, T. M., and Higurashi, A.: Improved hourly estimates of aerosol optical thickness using spatiotemporal variability derived from Himawari-8 geostationary satellite, IEEE Transactions on Geoscience and Remote Sensing, 56, 3442–3455, 2018.

Kim, B.-R., Kim, G., Cho, M., Choi, Y.-S., and Kim, J.: First results of cloud retrieval from the Geostationary Environmental Monitoring Spectrometer, Atmospheric Measurement Techniques, 17, 453–470, https://doi.org/10.5194/amt-17-453-2024, 2024.

Kim, M., Kim, J., Torres, O., Ahn, C., Kim, W., Jeong, U., Go, S., Liu, X., Moon, K., and Kim, D.-R.: Optimal Estimation-Based Algorithm to Retrieve Aerosol Optical Properties for GEMS Measurements over Asia, Remote Sensing, 10, 162, https://doi.org/10.3390/rs10020162, 2018.

Kuhlmann, G., Hartl, A., Cheung, H. M., Lam, Y., and Wenig, M.: A novel gridding algorithm to create regional trace gas maps from satellite observations, Atmospheric Measurement Techniques Discussions, 6, 7867–7910, https://doi.org/10.5194/amtd-6-7867-2013, 2013.

Liu, X., Chance, K., Sioris, C., Kurosu, T., Spurr, R., Martin, R., Fu, T.-M., Logan, J., Jacob, D., Palmer, P., Newchurch, M., Megretskaia, I., and Chatfield, R.: First Directly Retrieved Global Distribution of Tropospheric Column Ozone from GOME: Comparison with the GEOS-CHEM Model, Journal of Geophysical Research, 111, https://doi.org/10.1029/2005JD006564, 2006.

Loeb, N. G. and Manalo-Smith, N.: Top-of-atmosphere direct radiative effect of aerosols over global oceans from merged CERES and MODIS observations, Journal of Climate, 18, 3506–3526, 2005.

Lotrecchiano, N., Sofia, D., Giuliano, A., Barletta, D., and Poletto, M.: Spatial Interpolation Techniques For innovative Air Quality Monitoring Systems, Chemical Engineering Transactions, 86, 2021, https://doi.org/10.3303/CET2186066, 2021.

Matheson, M. A., Coakley Jr, J. A., and Tahnk, W. R.: Aerosol and cloud property relationships for summertime stratiform clouds in the northeastern Atlantic from Advanced Very High Resolution Radiometer observations, Journal of Geophysical Research: Atmospheres, 110, 2005.

Park, J., Kang, S., Jin, I. H., Kim, S., and Oh, D.: Geostationary Environment Monitoring Spectrometer (GEMS) User Manual Level – 3 Mean Field Algorithm, National Institute of Environmental Research, Republic of Korea, https://nesc.nier.go.kr/ko/html/satellite/guide/guide.do, 2023.

Park, S. S., Kim, S.-W., Song, C.-K., Park, J.-U., and Bae, K.-H.: Spatio-temporal variability of aerosol optical depth, total ozone and NO2 over East Asia: Strategy for the validation to the GEMS Scientific Products, Remote Sensing, 12, 2256, 2020.

Pöschl, U.: Atmospheric Aerosols: Composition, Transformation, Climate and Health Effects, Angewandte Chemie (International ed. in English), 44, 7520–40, https://doi.org/10.1002/anie.200501122, 2006.

Quarteroni, A., Sacco, R., and Saleri, F.: Numerical Mathematics, vol. 37, ISBN 978-1-4757-7394-1, https://doi.org/10.1007/b98885, 2007.

Shepard, D.: A Two-Dimensional Interpolation Function for Irregularly-Spaced Data, ACM National Conference, 23, 517–524, https://doi.org/10.1145/800186.810616, 1968.

Stocker, T.: Climate change 2013: the physical science basis: Working Group I contribution to the Fifth assessment report of the Intergovernmental Panel on Climate Change, 2014.

Tager, I.: Health effects of aerosols: Mechanisms and epidemiology, Aerosols Handbook: Measurement, Dosimetry, and Health Effects, 2013.

Tian, X., Tang, C., Wu, X., Yang, J., Zhao, F., and Liu, D.: The global spatial-temporal distribution and EOF analysis of AOD based on MODIS data during 2003–2021, Atmospheric Environment, 302, 119 722, 2023.

Webster, R. and Oliver, M. A.: Geostatistics for environmental scientists, John Wiley & Sons, 2007.

Zhang, F.: Factors Influencing the Spatio–Temporal Variability of Aerosol Optical Depth over the Arid Region of Northwest China, Atmosphere, 15, 54, 2023.

Zimmerman, D., Pavlik, C., Ruggles, A., and Armstrong, M. P.: An experimental comparison of ordinary and universal kriging and inverse distance weighting, Mathematical Geology, 31, 375–390, 1999.